

# Portal Vein and Hepatic Vein Segmentation in Multi-Phase MR Images Using Flow-Guided Change Detection

Qing Guo<sup>✉</sup>, Hong Song<sup>✉</sup>, Jingfan Fan<sup>✉</sup>, Danni Ai, Yuanjin Gao, Xiaoling Yu, and Jian Yang<sup>✉</sup>

**Abstract**—Segmenting portal vein (PV) and hepatic vein (HV) from magnetic resonance imaging (MRI) scans is important for hepatic tumor surgery. Compared with single phase-based methods, multiple phases-based methods have better scalability in distinguishing HV and PV by exploiting multi-phase information. However, these methods just coarsely extract HV and PV from different phase images. In this paper, we propose a unified framework to automatically and robustly segment 3D HV and PV from multi-phase MR images, which considers both the change and appearance caused by the vascular flow event to improve segmentation performance. Firstly, inspired by change detection, flow-guided change detection (FGCD) is designed to detect the changed voxels related to hepatic venous flow by generating hepatic venous phase map and clustering the map. The FGCD uniformly deals with HV and PV clustering by the proposed shared clustering, thus making the appearance correlated with portal venous flow robustly delineate without increasing framework complexity. Then, to refine vascular segmentation results produced by both HV and PV clustering, interclass decision making (IDM) is proposed by combining the overlapping region discrimination and neighborhood direction consistency. Finally, our framework is evaluated on multi-phase clinical MR images of the public dataset (TCGA) and local hospital dataset. The quantitative and qualitative evaluations show that our framework outperforms the existing methods.

**Index Terms**—Change detection, portal vein and hepatic vein, vascular segmentation, multi-phase MR images.

## I. INTRODUCTION

MULTI-PHASE magnetic resonance imaging (MRI) has rapidly become a standard imaging utility for liver

Manuscript received February 11, 2021; revised October 27, 2021 and January 30, 2022; accepted February 18, 2022. Date of publication March 11, 2022; date of current version March 21, 2022. This work was supported by the National Natural Science Foundation of China under Grant 62171039 and Grant 61771056. The associate editor coordinating the review of this manuscript and approving it for publication was Dr. Charles Kervrann. (*Corresponding authors:* Hong Song; Jingfan Fan.)

This work involved human subjects or animals in its research. Approval of all ethical and experimental procedures and protocols was granted by the Ethics Committee of Chinese PLA General Hospital under Approval No. S2020-464-01.

Qing Guo and Hong Song are with the School of Computer Science & Technology, Beijing Institute of Technology, Beijing 100081, China (e-mail: anniesun@bit.edu.cn).

Jingfan Fan, Danni Ai, and Jian Yang are with the School of Optics and Photonics, Beijing Institute of Technology, Beijing 100081, China (e-mail: jff@bit.edu.cn).

Yuanjin Gao is with the Department of Ultrasound, Beijing Children's Hospital, Capital Medical University, Beijing 100081, China.

Xiaoling Yu is with the Department of Interventional Ultrasound, Chinese PLA General Hospital, Beijing 100081, China.

Digital Object Identifier 10.1109/TIP.2022.3157136

lesions diagnosis and treatment due to its superiority of soft-tissue contrast and non-radiation exposure [1]. Segmenting portal vein (PV) and hepatic vein (HV) is a critical requirement for MRI-guided therapy procedures. The major reason is that HV and PV are commonly used to assist the liver segmental anatomy and locate the tumor position [2]. In addition, 3D segmentation results of HV and PV may help to reduce surgery risk of vessel injury whether for early liver resection treatment or currently minimally invasive therapeutic option [3]. However, positive PV and HV are fuzzy and noisy due to overlapping intensity and blurring edge issues. That is, the precise measurements of PV and HV are hampered by not only imaging limitation (i.e., the truncation artifacts and poor resolution), but also other tissues appearance (i.e., structure and texture information). More specifically, non-vascular tissues (e.g., tumor and hepatic parenchyma) on multi-phase MR images are significantly sensitive to contrast agent diffusion caused by blood flow event. As depicted in Fig. 1, late arterial phase (LAP) and portal venous phase (PVP), obtained by a time-setted system with standard MR protocol, present inhomogeneous contrast-enhanced appearance on various tissues.

Many methods have been proposed to delineate PV and HV. Existing approaches using single-phase data can be divided into tracing and deep learning based methods. The tracing-based methods were designed with a vascular continuity perspective. In [4], based on clustering results, PV and HV were automatically labelled by tracking per slice. This approach depended on the correctness of the initial slice and continuity of the clustering result. In [5], a centerline analysis method was added to connect the main vessel structure before tracking the slices along the z-axis. However, these slice-tracing methods assumed that the segmentation results of HV and PV are disconnected, without considering that they may actually be connected.

The centerline-tracing approaches utilize topological analysis to guide the delineation of HV and PV. Kang *et al.* [6] proposed a bottom-up vessel separation method, which starts with all the endpoints of the vessel centerline and traces the vascular roots by analyzing probability information between branches. Similarly to [6], Zeng *et al.* [7] chose leaf nodes as the start points and traversed them along the height ridge of vessel to identify HV and PV structure. Based on graph idea, Yan *et al.* [8] determined the category of vascular branches by modelling each neighborhood of vessel intersection (adhesion

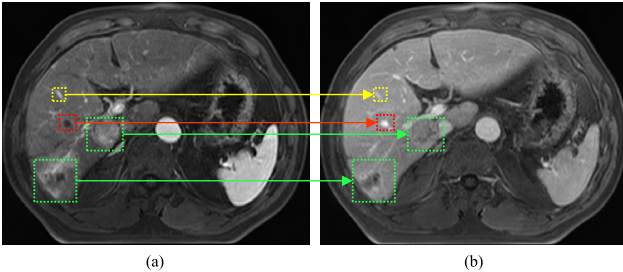


Fig. 1. Example of LAP and PVP image. (a) LAP image in the axial plane. (b) The corresponding PVP image. The red, yellow, and green dotted box demonstrate appearance related to hepatic venous flow, portal venous flow, and tumor region, respectively. The red, yellow, and blue arrow point from LAP to PVP image, and respectively indicate the corresponding change.

part of HV and PV segmentation result) and analyzing its local features. The continuity of vessel segmentation needs to be ensured for this method, thus requiring human intervention. The critical challenge of the above tracing-based methods is difficult to clearly define a wide range of intersection cases while analyzing the topological relationships between HV and PV. Notably, only abdominal computed tomography (CT) images were discussed in these approaches. Compared with CT images, the performance of topological analysis on MR images may be limited by irregular tubular shape and unconventional bifurcation structure, due to the imaging limitation and tissue appearance abundance of MRI (e.g. Fig. 1).

Recently, deep learning-based methods have achieved some advancement in HV and PV segmentation. Yu *et al.* [9] employed residual modules with the 3D-UNet to segment the HV and PV on 109 abdominal clinical CT volumes. Ivashchenko *et al.* [10] proposed a new V-Net, which combines residual dense block and dilated convolution, to segment HV and PV. This network trained with a focal loss function has achieved good results on the MR image segmentation task. Exploring the topological relationship between HV and PV helps to segment two kinds of vasculatures more precisely, especially when their characters (e.g. structure and texture information) are similar in the local region on single-phase data. For this, Keshwani *et al.* [11] proposed a novel topology metric learning by using a multi-task architecture to achieve CT-based HV and PV segmentation, yet multiple parameters were required to fine-tune manually.

Compared with single phase-based approaches, multiple phases-based approaches have better scalability in distinguishing HV and PV by using multi-phase information. Alhonnoro *et al.* [12] developed a semi-automatic tool based on Hessian-based vessel enhancement and ridge-oriented region growing for vessel segmentation. In porcine livers, the arterial, PV, and HV were segmented from three-phase contrast-enhanced CT images. Ivashchenko *et al.* [13] proposed an automatic segmentation method, in which vessel enhancement is combined with automatic thresholding method to extract HV, PV, and biliary ducts. The main branches of HV and PV were experientially distinguished by cluster size.

Although these approaches are effective and scalable for the segmentation task of HV and PV, they are hard to capture the real structure of target vasculature. More specifically, they tend to yield HV and PV segmentation only according to the enhancement feature on different phase images, while the change and appearance caused by the vascular flow event are ignored.

In this paper, the issue of delineating the change is addressed by introducing change detection (CD) model. As a powerful model for capturing change information, CD aims at detecting changed objects from two input images acquired at two distinct moments in the same position. Thus, a favorable foundation is supported by CD for estimating changes caused by the vascular flow event between two distinct phase images. Differing from general CD, our work tends to detect the change related to hepatic venous flow instead of all changes caused by the vascular flow event. To this end, we propose a novel CD model, flow-guided change detection (FGCD), to make HV voxels more distinguishable. Similar to the universal CD model, FGCD includes two main procedures after pre-processing: difference map generation, and difference image analysis. Firstly, a generation module is designed to hepatic venous phase (HVP) map between the pre-processed LAP and PVP images. Secondly, inspired by the solution to unbalanced cluster-size and non-spherical data problem in the segmentation of 2D MR images [14], we utilize the similarity-based fuzzy clustering to analyze changed voxels related to hepatic venous flow. To robustly delineate the appearance correlated with portal venous flow without increasing framework complexity, we develop a shared clustering module. Our shared clustering computes the probability of vascular (resp. changed) and non-vascular (resp. non-changed) voxels based on similarity measurement. Compared with [14], a parameter-sharing strategy and vascular prior space constraint are supplemented in our module. In the iterative process of HV (resp. PV) clustering, the clustering of HV (resp. PV) voxels depends on the voxels with similar appearance related to hepatic (resp. portal) venous flow instead of all voxels with similar appearance in the liver. However, some noisy regions may remain in the HV and PV clustering results, because of the incorrect contrast-enhanced appearance in HV and PV during different phases. This issue can be explained by different patient selection to some extent. Therefore, to obtain refinement segmentation results of HV and PV, interclass decision making (IDM) is proposed by combining of overlapping region discrimination and neighborhood direction consistency.

Our work makes four-fold major contributions:

- We propose a framework to solve the 3D HV and PV segmentation problem by leveraging characters such as structure and texture information of intrahepatic tissue on multi-phase images caused by the vascular flow event, and their differences. Our framework can capture the real structures of target vasculature (HV or PV) through analyzing this information.
- We introduce a parameter-sharing strategy that can cluster both HV and PV voxels by establishing 3D vascular prior space to constrain the spatial similarity

calculation. With the decision-making between HV and PV categories, our framework achieves more integral refinement segmentation results.

- We design a novel CD model, named flow-guided change detection (FGCD), which can detect the changed voxels related to hepatic venous flow instead of all changes caused by the vascular flow event.
- Experimental results on clinical datasets, including public and private datasets, demonstrate the effectiveness of our framework in segmenting HV, PV, and intrahepatic vasculature both quantitatively and qualitatively.

The rest of this paper is organized as follows. Some background knowledge about CD and a review of vascular segmentation methods on MR images are presented in Section II. The proposed FGCD and IDM are introduced in Section III. In Section IV, the proposed method is evaluated by real-patient multi-phase MR images of the public dataset and local hospital dataset. The conclusion is provided in Section V.

## II. RELATED WORKS

This section introduces some background about CD, and provides a brief review about vascular segmentation methods on MR images considering the limited studies for intrahepatic vasculature segmentation on MR images.

CD is explicitly of great significance in both natural and medical images [15]. The core issue of CD is the recognition and segmentation of difference regions between two co-registered images. For natural images, Zheng *et al.* [16] proposed a new difference image generation method, which combines the local consistency with edge information through a regularization parameter. Shao *et al.* [17] adopted a strategy of synergizing three kinds of information (e.g., intensity level, label and spatial background) extracted from difference image, and designed a robust semi-supervised fuzzy C-means (FCM) clustering algorithm. Zheng *et al.* [18] utilized the saliency information of the difference image as prior knowledge to guide the extraction of the change feature, and k-means clustering is employed to detect the change object. Liu *et al.* [19] proposed the homogeneous pixel transformation method to set up mappings between the input domains and other domains and employed the FCM clustering method to divide the difference values into changed and non-changed pixels. Liu *et al.* [20] designed morphological denoise method before generating the difference map to preserve image details and obtained the CD results by using k-means clustering. For medical images, CD is explored in the MR images field because of the rich imaging information of soft tissues. Lesjak *et al.* [21] captured the change features of white matter lesions because of the evolution of lesions. Dufresne *et al.* [22] considered the brain difference caused by atrophy and proposed a framework in which the deformation registration and CD are conciliated.

Vessel segmentation on MR images can be realized using some methods. Goceri *et al.* [23] proposed an adaptive and reconstructive method of vessel segmentation in each slice after k-means initial clustering. Virzi *et al.* [24] extracted and

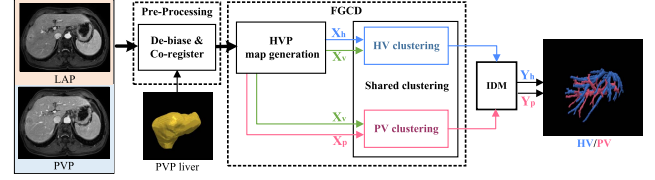


Fig. 2. A flowchart of the proposed framework FGCD-IDM is illustrated. The black dotted box represents our proposed FGCD, the blue arrow represents the HV clustering (blue box) pipeline, and the pink arrow represents the PV clustering (pink box) pipeline.  $X_h$  represents the filtered HVP image by JFMS;  $X_p$  and  $X_h$  represent the pre-processed PVP and LAP image after JFMS filtering, respectively;  $Y_h$  represents HV segmentation; and  $Y_p$  represents PV segmentation.

combined 2D axial patches used as input for a convolutional neural network from T2 weighted MR images. The semi-automatic method needed some user-selected landmarks to assist in pelvic vessel segmentation. Tetteh *et al.* [25] proposed DeepVesselNet by utilizing 2D orthogonal cross-hair filters and introducing 3D context information, which reduced computational cost. Zhao *et al.* [26] proposed a semi-supervised method to segment cerebrovascular though the hierarchical update of CNN. However, collecting data for supervised training is laborious, and densely labelling 3D vascular ground-truth is difficult [27]. Zhou *et al.* [27] adopted Gaussian mixture model (GMM) as a low-level process and a new potential function of pair-wise sites based on the Markov neighborhood system as a high-level process to segment cerebrovascular. The cluster-number of low-level process was fixed and suitable for cerebrovascular data where intensity distribution changes slightly [28].

## III. METHOD

Herein, we formulate the HV and PV sync-segmentation problem in a unified framework named FGCD-IDM, as illustrated in Fig. 2. Let  $I_p$  and  $I_b$  be a pair of LAP-PVP images acquired at two set times. First of all, the pair LAP-PVP images are de-biased by N4 bias field correction algorithm [29] and co-registered (PVP as reference and LAP as floating) by the non-rigid registration method [30] based on liver region  $\Gamma$  (binary mask), such as (a) and (c) shown in Fig. 3. After the above pre-processing, the FGCD detects HV and PV via two tightly integrated modules, namely HVP map generation and shared clustering module. Finally, the refinement segmentation results of HV and PV are obtained by IDM.

### A. HVP map Generation

The difference map generation of CD usually works with various operators to effectively utilize their advantages. A combined difference map [16] can be defined as follows:

$$O = \mathcal{MD}(\zeta O_r + (1 - \zeta) O_s), \quad (1)$$

where operators  $O_s$  and  $O_r$  are normalized to the range [0,1]. The regularization parameter  $\zeta$  balances the weight of the two operators. To preserve edges and remove isolated noise, a median filter  $\mathcal{MD}(\cdot)$  is adopted on  $O$ .

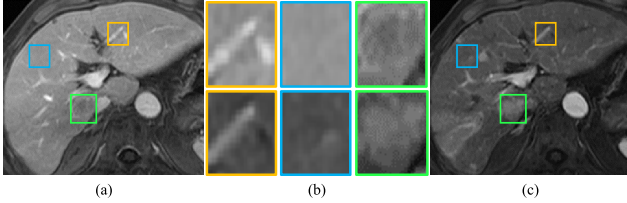


Fig. 3. Examples of appearance correlation on co-registered LAP-PVP image after pre-processing. (a) pre-processed PVP image. (c) pre-processed LAP image. (b) patches amplify for display the colored boxes in (a) and (c). The left column (orange) patches of (b) show the example of the vascular mutual structures between the (a) and (c). The middle column patches (blue) of (b) depict example of the smooth parenchyma regions between the two images. The right column (green) patches of (b) depict example of the inconsistent pathology structures between the two images.

Generally, PV is opacified during LAP, and whole hepatic vasculature is enhanced during PVP under standard MRI protocol [31]. To highlight the change related to hepatic venous flow between the LAP and PVP images (e.g. Fig. 1), the subtraction operator  $O_s$  and ratio operator  $O_r$  are constructed as follows:

$$O_s = \text{sign}(X_1 - X_2) \max(X_1 - X_2, 0) \quad (2)$$

$$O_r = \frac{X_1}{X_2 + \Delta}, \quad (3)$$

where  $\Delta$  is a small number and used to avoid zero denominator in (3). The quantitative analysis of the regularization parameter  $\zeta$  is provided in Section IV-B.

Although the LAP and PVP images have been co-registered after pre-processing, their appearance are not exactly consistent. Similar to [32], three kinds of differences between co-registered LAP-PVP images can be presented, including 1) *vascular mutual structures*: common vascular edges, which are not necessarily with the same magnitude and gradient direction between the two patches, as shown in the left column patches of Fig. 3(b); 2) *smooth parenchyma regions*: low-variance smooth patches in the liver region with fuzzy artifacts and noise, as shown in the middle column patches of Fig. 3(b); 3) *inconsistent pathology structures*: distinct patterns between the two patches, including one pathology edge that appears on the LAP image but not on the PVP image, as shown in the right column patches of Fig. 3(b). Based on the three definitions, the pre-processed LAP image  $I'_p$  and PVP image  $I'_v$  are filtered by joint filtering through using mutual structure (JFMS [32] with the image  $I'_v$ ) to obtain the images  $X_p$  and  $X_v$  reducing the fuzzy artifacts and noise. Then, the combined difference map as HVP image is given by (1) with the two constructed operators ((2) and (3)). The inputs of the two operators are  $\hat{X} = \{X_1 = X_v, X_2 = X_p\}$ . Finally, the HVP image filtered by JFMS with the guidance image  $I'_v$  to yield the image  $X_h$ . This guidance process is highly relative to the following difference analysis step for mitigating the effect of pseudo-vascular noise caused by the vascular flow event. A detailed discussion is presented in Section IV-B.

## B. Shared Clustering

The similarity-based clustering algorithm adopting the intraclass and interclass similarity can suppress the sensitivity to unbalanced cluster-size in 2D [14]. The cost for shared clustering is a 3D extension of 2D similarity-based method with integrated the vascular prior space constraint. We formulate the PV and HV sync-clustering problem by using a parameter-sharing strategy, which can deal with both HV and PV clustering in a unified manner. Without loss of generality, the following discussion takes the cost for shared clustering on filtered HVP image  $X_h$ , i.e., HV clustering, as an example:

1) *Cost for Shared Clustering*: Let  $K$  be the number of clusters and  $\Phi^h$  be a 3D vascular prior space. The objective function of the shared clustering method is obtained as follows:

$$\mathcal{J}_h = \sum_{k=1}^K \sum_{n=1}^{|\Phi^h|} \left[ a \left( u_{kn}^h \right)^\alpha + b \left( t_{kn}^h \right)^\beta \right] \cdot \frac{1}{(r_{kn}^h)^2} + \sum_{k=1}^K \eta_k^h \sum_{n=1}^{|\Phi^h|} \left( 1 - t_{kn}^h \right)^\beta, \quad (4)$$

subject to  $u_{kn}^h, t_{kn}^h \in [0, 1]$  and  $\sum_{k=1}^K u_{kn}^h = 1$  for all  $n = 1, \dots, |\Phi^h|$ , where  $|\cdot|$  denotes the cardinality of a set.  $u_{kn}^h$  and  $t_{kn}^h$  are the membership and typicality of possibilistic FCM (PFCM) and are represented with the partition matrix  $U_h = [u_{kn}^h]_{K \times |\Phi^h|}$  and  $T_h = [t_{kn}^h]_{K \times |\Phi^h|}$ .  $r_{kn}^h$  expresses spatial similarity measure.  $a$  and  $b$  are considered as the relative importance measurement factors for FCM and PCM [33]. Fuzzy factors  $\alpha$  and  $\beta$  are equal and usually set as 2. The weight  $\eta_k^h$  is the user-defined constant calculated by the initial membership and the initial center [34].

With an aim not to miss vascular voxels, the vascular prior space  $\Phi^h$  is acquired by closing and dilating the binarization of vascular prior response. The vascular prior response  $\tilde{V}_h$ , based on the general vessel enhancement response [35], is designed by jointing with the combination of distribution statistics and gradient suppression information from both the HVP and PVP image, and defined as follows:

$$\tilde{V}_h = \max_{\delta_{\min} \leq \delta \leq \delta_{\max}} V_h(\delta) M_h M_v W_h^{\frac{\phi}{2}}(\delta) W_v^{\frac{\varphi}{2}}(\delta), \quad (5)$$

where  $V_h(\delta)$  is the general vessel enhancement response at each scale  $\delta$  ( $\delta_{\min} \leq \delta \leq \delta_{\max}$ ) corresponding to the HVP image.  $M_h$  (resp.  $M_v$ ) and  $W_h(\delta)$  (resp.  $W_v(\delta)$ ) express the distribution statistics and gradient suppression information counterparts to the HVP (resp. PVP) image, respectively. Factor  $\phi$  (resp.  $\varphi$ ) controls the suppression range of  $W_h(\delta)$  (resp.  $W_v(\delta)$ ). Similar to [36], the boundary expansion images  $E_h$  and  $E_v$ , instead of  $X_h$  and  $X_v$ , are utilized as inputs in (5) to mitigate undesired strong contrast near the liver boundary. The details of distribution statistics and gradient suppression in (5) are explained below:

*Distribution statistics*: GMM can yield the statistical information regarding vascular distribution [27]. Based on

inputs  $E_v$  and  $E_h$ ,  $M_v$  and  $M_h$  can be calculated by:

$$M(s_n) = 1 - \sum_{i=1}^J \omega_j \mathcal{N}(E(s_n) | \mu_j, \sigma_j), \quad (6)$$

where  $\mathcal{N}$  is the  $j$ th component of GMM, and the optimal component number  $J$  is automatically selected by the Bayesian information criterion. The parameters  $(\omega_j, \mu_j, \sigma_j)$  of this model are estimated via k-means pre-clustering and iteratively obtained using the expectation maximisation algorithm.

*Gradient suppression:* For a sizable scale  $\delta$ , under which gradient diffusion on non-vascular regions with large curvatures may occur, we propose the gradient suppression to reduce a considerable response  $V_h(\delta)$  caused by the gradient diffusion. The gradient suppression  $W(\delta)$  is expressed as:

$$W(\delta) = 1 - \frac{2}{\pi} \arctan \left( \frac{G(\delta) - g(\delta)}{\max_{s_n} G(\delta)} \gamma \right), \quad (7)$$

where  $\gamma$  is the curvature coefficient of (7) and sets as 2.  $W_h(\delta)$  (resp.  $W_v(\delta)$ ) is calculated by (7) with the gradient map  $G_h(s_n, \delta) = f'(E_h(s_n)\Gamma(s_n), \delta)$  (resp.  $G_v(s_n, \delta) = f'(E_v(s_n)\Gamma(s_n), \delta)$ ) and the gradient threshold  $g_h(\delta) = Otsu(G_h(\delta))$  (resp.  $g_v(\delta) = Otsu(G_v(\delta))$ ). Considering the case of the main vascular branches with large gradients, the corresponding conditions  $\phi$  and  $\varphi$  of (5) are designed to control the suppression  $W_h(\delta)$  and  $W_v(\delta)$ , respectively, and defined as follows:

$$\begin{aligned} \phi &= \text{sign}[x_h - X_h] - \text{sign}(g_h(\delta) - G_h(\delta)) - 1] + 1 \\ \varphi &= \text{sign}[\text{sign}(x_v - X_v) - \text{sign}(g_v(\delta) - G_j(\delta)) - 1] + 1, \end{aligned} \quad (8)$$

where  $x_h = Otsu(\mathcal{MIP}(X_h))$  and  $x_v = Otsu(\mathcal{MIP}(X_v))$ .  $\mathcal{MIP}$  indicates the maximum intensity projection in the z-axis direction. The  $\phi$  or  $\varphi$  controls  $W_h(\delta)$  or  $W_v(\delta)$  not to inhibit the response of major vascular branches, when  $X_h$  or  $X_v$  is higher than the intensity condition  $x_h$  or  $x_v$ .

Based on 3D vascular prior space  $\Phi^h$ , spatial similarity measure is denoted by  $r_{kn}^h$ , as follows:

$$r_{kn}^h = \sum_{q=1}^K \frac{\sum_{n \in \Lambda} \rho_{kn}^h \rho_{qn}^h}{\sqrt{\sum_{n \in \Lambda} \rho_{kn}^h \sum_{n \in \Lambda} \rho_{qn}^h}} \cdot \rho_{qn}^h, \quad (9)$$

where  $R_h = [r_{kn}^h]_{K \times |\Phi^h|}$  is the spatial similarity matrix. To make the voxels involved in similarity calculation more representative, we utilize the constraint  $\Lambda = \{n | \arg \max \{\rho_{kn}^h, \rho_{qn}^h\}\}$  to  $R_h$  in (9). Compared with the literature [14], this paper establishes the spatial similarity relationship more consistent with similar appearance related to vascular flow. The spatial relative similarity  $\rho_{kn}^h$  is obtained by the correlation function combined with the intensity

information  $D_{nl}^h$  and spatial information  $L_{nl}^h$  as follows:

$$\rho_{kn}^h = \frac{\sum_{l \in \Omega_l} [a(u_{kl}^h)^\alpha + b(t_{kl}^h)^\beta] \exp(D_{nl}^h + L_{nl}^h)}{\sum_{l \in \Omega_l} [a(u_{kl}^h)^\alpha + b(t_{kl}^h)^\beta] + \Delta} \quad (10)$$

$$D_{nl}^h = \frac{-|X_h(s_n) - X_h(s_l)|^2}{H_h^2} \quad (11)$$

$$L_{nl}^h = \frac{-\|s_n - s_l\|^2}{B_h}, \quad (12)$$

where  $B_h$  is the diagonal length of the bounding box of the space  $\Phi^h$ ,  $H_h$  is the bandwidth [37], and  $\Omega_l = \{l | |X_h(s_n) - X_h(s_l)| < \epsilon, s_l \in \Phi^h\}$  is the similarity range. The quantitative analysis of the effect of the parameter  $w$  of  $\epsilon = w/|\Phi^h| \sum_{n=1}^{|\Phi^h|} |X_h(s_n) - 1/|\Phi^h| \sum_{n=1}^{|\Phi^h|} X_h(s_n)|$  is provided in Section IV-C.

*2) Iterative Minimization of the Cost:* The objective function  $\mathcal{J}_h$  could be minimized using the Lagrange method. First,  $\tilde{\mathcal{J}}_h$  with a coefficient  $\lambda_n$  is employed as follows:

$$\begin{aligned} \tilde{\mathcal{J}}_h &= \sum_{k=1}^K \sum_{n \in \Phi^h} \left[ a(u_{kn}^h)^\alpha + b(t_{kn}^h)^\beta \right] \cdot \frac{1}{(r_{kn}^h)^2} \\ &\quad + \sum_{k=1}^K \eta_k^h \sum_{n \in \Phi^h} (1 - t_{kn}^h)^\beta + \sum_{n \in \Phi^h} \lambda_n \left( 1 - \sum_{k=1}^K u_{kn}^h \right). \end{aligned} \quad (13)$$

Then, the derivative of  $\tilde{\mathcal{J}}_h$  with respect to  $u_{kn}^h$ ,  $t_{kn}^h$  and  $\lambda_n$  is obtained, and the results are set to 0. At each loop counter  $m$ , we calculate the membership  $u_{kn}^{h(m)} \in U_h^{(m)}$  and the typicality  $t_{kn}^{h(m)} \in T_h^{(m)}$  as follows:

$$u_{kn}^{h(m+1)} = \frac{(r_{kn}^{h(m)})^{\frac{2}{\alpha-1}}}{\sum_{k=1}^K (r_{kn}^{h(m)})^{\frac{2}{\alpha-1}}} \quad (14)$$

$$t_{kn}^{h(m+1)} = \frac{1}{1 + \left( \frac{\sqrt{b}}{\sqrt{\eta_k^h r_{kn}^{h(m)}}} \right)^{\frac{2}{\beta-1}}}. \quad (15)$$

In addition, to reduce the sensitivity to noise, the local information is considered by initializing the membership from vascular prior response. The FCM is a simple clustering method, which is employed to initialize the membership  $U_h^{(0)}$  of the response  $\tilde{V}_h$  and generate the candidate binarization region. In class  $k$ , we assume that  $u_{kn}^h \in U_h$  and  $t_{kn}^h \in T_h$  are the final membership and typicality, respectively. The final possibility  $p_{kn}^h$  represented with the probabilistic matrix  $P_h = [p_{kn}^h]_{K \times |\Phi^h|}$  is defined as:

$$p_{kn}^h = au_{kn}^h + bt_{kn}^h, \quad (16)$$

For all  $s_n \in \Phi^h$ , and  $\forall k = 1, \dots, K$ .

In PV clustering, except for different input image  $X_p$ , the response  $\tilde{V}_p$ , space  $\Phi^p$ , and iterative minimization of the cost  $\mathcal{J}_p$  follows the same way as that for  $\tilde{V}_h$ ,  $\Phi^h$  and  $\mathcal{J}_h$  as discussed above. The shared clustering (i.e., HV and PV

**Algorithm 1:** Framework of FGCD-IDM

**Input:** Pre-processed LAP and PVP images:  $I'_p$ ,  $I'_v$   
the liver region:  $\Gamma$

**Output:** Binary HV and PV segmentation results:  $Y_h$ ,  $Y_p$

**1. HVP Map Generation Step**

- $X_v, X_p \leftarrow$  filter  $I'_p$  and  $I'_v$  via JFMS with  $I'_v$
- $O_s \leftarrow \text{sign}(X_v - X_p) \max(X_v - X_p, 0)$
- $O_r \leftarrow X_v / (X_p + \Delta)$
- Calculate  $O$  using (1), regularization param.  $\zeta = 0.3$
- $X_h \leftarrow$  filter  $O$  via JFMS with  $I'_v$

**2. Shared Clustering Step**

▷ Shared param.:

$$K \leftarrow 2, \kappa \leftarrow 10^{-3}, w \leftarrow 1.75, a \leftarrow 0.65, b \leftarrow 1 - a, \mathfrak{M} \leftarrow 200$$

▷ HV Clustering:

- Calculate  $V_h$  using (5) with  $X_h$  and  $X_v$
- Initialize  $U_h^{(0)}$  via FCM with  $V_h$ , and  $T_h^{(0)}$  randomly
- Establish  $\Phi^h$ ,  $m \leftarrow 0$

**while**  $err > \kappa$  and  $m < \mathfrak{M}$  **do**

- Calculate  $R_h^{(m)}$  using (9)-(12) with  $X_h$
- Calculate  $U_h^{(m)}$  using (14) and  $T_h^{(m)}$  using (15)
- $err \leftarrow \|U_h^{(m)} - U_h^{(m-1)}\|_2$ ,  $m \leftarrow m + 1$
- $U_h \leftarrow U_h^{(m+1)}$ ,  $T_h \leftarrow T_h^{(m+1)}$
- Calculate  $P_h$  using (16)

▷ PV Clustering:

- Calculate  $V_p$  using (5) with  $X_p$  and  $X_v$
- Initialize  $U_p^{(0)}$  via FCM with  $V_p$ , and  $T_p^{(0)}$  randomly
- Establish  $\Phi^p$ ,  $m \leftarrow 0$

**while**  $err > \kappa$  and  $m < \mathfrak{M}$  **do**

- Calculate  $R_p^{(m)}$  using (9)-(12) with  $X_p$
- Calculate  $U_p^{(m)}$  using (14) and  $T_p^{(m)}$  using (15)
- $err \leftarrow \|U_p^{(m)} - U_p^{(m-1)}\|_2$ ,  $m \leftarrow m + 1$
- $U_p \leftarrow U_p^{(m+1)}$ ,  $T_p \leftarrow T_p^{(m+1)}$
- Calculate  $P_p$  using (16)

**3. Interclass Decision Making Step**

▷ Initialization: Label  $S^q$  based on  $P_p$  and  $S^r$  based on  $P_h$

▷ HV Refinement:

- $C^q \leftarrow S^q$ ,  $C^r \leftarrow S^r$

**foreach**  $c_i^q$  in  $C^q - \{c_1^q\}$  **do**

- if  $\mathbb{C}(c_j^r, c_i^q) \neq \emptyset$  **then**
- Calculate  $\Omega_i$  using (23)
- Update  $\tilde{C}^r$  using  $C^r \cup \Omega_i$  and  $\tilde{C}^q$  using  $C^q - \Omega_i$

- $\tilde{S}^r \leftarrow \tilde{C}^r$ ,  $\tilde{S}^q \leftarrow \tilde{C}^q$
- $Y_h \leftarrow \tilde{S}^r$

▷ PV Refinement:

- $C^q \leftarrow S^r$ ,  $C^r \leftarrow \tilde{S}^q$

**foreach**  $c_i^q$  in  $C^q - \{c_1^q, c_2^q\}$  **do**

- if  $\mathbb{C}(c_j^r, c_i^q) \neq \emptyset$  **then**
- Calculate  $\Omega_i$  using (23)
- Update  $\tilde{C}^r$  using  $C^r \cup \Omega_i$  and  $\tilde{C}^q$  using  $C^q - \Omega_i$

- $\tilde{S}^q \leftarrow \tilde{C}^q$ ,  $\tilde{S}^r \leftarrow \tilde{C}^r$
- $Y_p \leftarrow \tilde{S}^r$

clustering) can be demonstrated as the following pseudocode in Algorithm 1. In the implementation process of Algorithm 1,

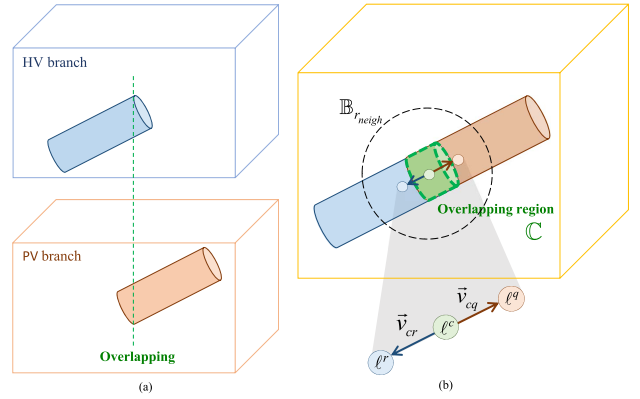


Fig. 4. (a) The overlapping case of HV and PV segmentation results. (b) overlapping region discrimination strategy utilizes the average membership of the overlapping region (green), and neighborhood direction consistency strategy analyzes the parallelism of the vector  $\vec{v}_{cr}$  and  $\vec{v}_{cq}$  in the spherical region (dashed circle).

two strategies are used to reduce the computational time of the three-dimensional clustering: establishment of the vascular prior space and thread-based way. The vascular prior space based on vascular prior response could not only resolve the uncertain cluster-number problem, but can also reduce the computational time of the shared clustering because computational size is far less than that of the original input data. The calculation of similarity  $\rho_{kn}^h$  and  $\rho_{kn}^p$  is conducted using thread-based Cython (<http://cython.org>).

### C. Interclass Decision Making

Without loss of generality, HV and PV clustering are independently implemented on different images, that is, their segmentation results can be regarded as two disjoint sets. However, the concrete situation may be extremely complicated, e.g., the HV end branches are visible on LAP image, making the two disjoint sets liable to overlapping in some same positions. The overlapping case can be shown in Fig. 4(a).

So we intend to refine the segmentation results obtained from HV and PV probabilistic matrixes according to the overlapping regions and their neighborhood information. Let  $C^r = \{c_j^r\}_{j=1}^{|C^r|}$  represent all independent connected regions of segmentation result  $S^r = \{s_n^r\}_{n=1}^{|S^r|}$  for  $|C^r|$  regions as a record candidate set, while  $C^q = \{c_j^q\}_{j=1}^{|C^q|}$  represents those of segmentation result  $S^q = \{s_n^q\}_{n=1}^{|S^q|}$  for the corresponding  $|C^q|$  regions as a query candidate set, where  $s_n^r$  (resp.  $s_n^q$ ) and  $c_j^r$  (resp.  $c_j^q$ ) are a voxel and a connected region, respectively.  $j$  is lexicographically ordered and inversely proportional to the number of voxels in a connected region. According to the above definition, the two strategies below are used to address the above overlapping problem.

1) *Overlapping Region Discrimination:* If a certain number of overlapping voxels of a connected region have clear subordination (HV/PV category), their adjacent voxels of the region should also have the same subordination. Therefore, the discrimination problem of each independent connected region

belonging to the query candidate set is transformed into that of each common region formed by the intersection of query and the record candidate sets (Fig. 4(b)). The overlapping region is defined as follows:

$$\mathbb{C}(c_j^r, c_i^q) = \{s_n^r, s_n^q | s_n^r, s_n^q \in c_j^r \cap c_i^q, \forall j = 1, \dots, |C^r|, \forall i = m, \dots, |C^q|, m \in \{2, 3\}\}, \quad (17)$$

where  $m = 2$  represents the exclusion of a maximum region in HV refinement, and  $m = 3$  denotes the exclusion of the first two maximum regions in PV refinement.  $s_n^r$  and  $s_n^q$  are two overlapping voxels. To discriminate the subordination of one independent connected regions, we compare the average memberships of the overlapping region belonging to the query candidate set and that belonging to the record candidate set.  $\bar{u}_K^q$  and  $\bar{u}_K^r$  are defined as follows:

$$\bar{u}_K^q = \frac{1}{|\mathbb{C}(c_j^r, c_i^q)|} \sum_{\{n | s_n^q \in \mathbb{C}(c_j^r, c_i^q)\}} u_{Kn}^q \quad (18)$$

$$\bar{u}_K^r = \frac{1}{|\mathbb{C}(c_j^r, c_i^q)|} \sum_{\{n | s_n^r \in \mathbb{C}(c_j^r, c_i^q)\}} u_{Kn}^r. \quad (19)$$

2) *Neighborhood Direction Consistency*: In actual situation, if the overlapping voxels are a few, overlapping region discrimination may be inadequate to support the clear subordination of the corresponding connected region. From complementary perspectives, we propose a neighborhood direction consistency strategy. We create a spherical region  $\mathbb{B}_{r_{neigh}}(\ell^c)$  with radius  $r_{neigh}$  around the centroid  $\ell^c$  of the overlapping region and construct two vectors (i.e.  $\vec{v}_{cr}(\ell^r, \ell^c)$  and  $\vec{v}_{cq}(\ell^q, \ell^c)$ ). The location  $\ell^c$ ,  $\ell^r$ , and  $\ell^q$  are defined as follows:

$$\ell^c = \frac{1}{|\mathbb{C}(c_j^r, c_i^q)|} \sum_{\{n | s_n^r \in \mathbb{C}(c_j^r, c_i^q)\}} s_n^r \quad (20)$$

$$\ell^r = \frac{1}{|\mathbb{B}_{r_{neigh}}(\ell^c) \cap c_j^r|} \sum_{\{n | s_n^r \in \mathbb{B}_{r_{neigh}}(\ell^c) \cap c_j^r\}} s_n^r \quad (21)$$

$$\ell^q = \frac{1}{|\mathbb{B}_{r_{neigh}}(\ell^c) \cap c_i^q|} \sum_{\{n | s_n^q \in \mathbb{B}_{r_{neigh}}(\ell^c) \cap c_i^q\}} s_n^q. \quad (22)$$

where  $\ell^r$  and  $\ell^q$  are the region centroid of the two sets in the  $\mathbb{B}_{r_{neigh}}(\ell^c)$ , respectively. The neighborhood direction consistency depends on the parallelism of the two vectors based on a cosine distance, as shown in Fig. 4(b).

In summary, a proper and robust approach is the combination of overlapping region discrimination and neighborhood direction consistency to update the record candidate set  $\tilde{C}^r = C^r \cup \Omega_i$  and the query candidate set  $\tilde{C}^q = C^q - \Omega_i$  when traversing the  $i$ th region, as demonstrated in Algorithm 1. The refinement region  $\Omega_i$  is defined as:

$$\Omega_i = \{c_i^q | \bar{u}_K^r > \bar{u}_K^q \text{ and } |\cos(\langle \vec{v}_{cr}(\ell^r, \ell^c), \vec{v}_{cq}(\ell^q, \ell^c) \rangle)| > 0.5\}, \quad (23)$$

where  $\vec{v}_{cr}(\ell^r, \ell^c) = \ell^r - \ell^c$  and  $\vec{v}_{cq}(\ell^q, \ell^c) = \ell^q - \ell^c$ .

#### IV. EXPERIMENTS AND ANALYSIS

In this section, we evaluate the performance of our framework. We first describe the datasets and evaluation metrics utilized in our paper (Section A). Then, our proposed framework is evaluated based on three aspects, namely, the FGCD study (Section B), the evaluation of segmentation performance (Section C), the evaluation of separation performance (Section D), and the robustness discussion (Section E).

##### A. Datasets and Evaluation Metrics

1) *Clinical MRI Datasets*: The proposed framework was evaluated on two datasets of clinical multi-phase MR images. The Local Hospital Dataset (LHD) was collected in our collaboration with PLA General Hospital to study preoperative planning. The LHD contains 30 clinical MR volumes from 15 patients with 15 LAP and 15 PVP. These MR volumes are selected from 3D T1-weighted sequences (FS, mDIXON, LAVA, or LAVA-Flex) which are acquired under standard MRI protocols after intravenously gadolinium-based contrast agent. LHD has a voxel size of  $0.78 \times 0.78 \times 2.5 \text{ mm}^3$ . The clinical MR volumes of the LHD are obtained using 6 different scanners, with UIH uMR (560, 570, and 770), Philips Multiva, GE Discovery MR750 and GE Signa HDxt. The matrix dimension of these volumes includes  $87 \times 511 \times 409$ ,  $83 \times 319 \times 319$ ,  $79 \times 511 \times 511$ , and  $87 \times 511 \times 311$ . Considering the difference in MRI caused by the manifold acquisition situations (e.g., MR technology, and resolution setting), we added another dataset to test and analyze the segmentation performance of HV and PV. The public dataset was obtained from The Cancer Genome Atlas dataset (TCGA, <https://cancergenome.nih.gov/>) which contains a few abdomen MR images involving multiple phases. However, TCGA is not a dedicated and open MRI dataset for vessel segmentation. To qualitatively and quantitatively verify the generalizability of our framework, we determined two LAP data and two PVP data of TCGA and tested them in the optimum condition of LHD experiment (i.e., Section C). These data of TCGA are acquired on Philips Ingenia and Siemens Aera scanner. The voxel sizes of these data are  $1.125 \times 1.125 \times 2.5 \text{ mm}^3$  and  $1 \times 1 \times 1.75 \text{ mm}^3$ .

The above PVP data were all manually segmented by an experienced radiologist to delineate the PV, HV, and liver regions. To avoid annotation mistakes of HV and PV by the expert, another two experienced radiologists as independent observers participated in this task. They performed the delineations by following the common and agreed-upon instructions in the guidelines. The observers checked and corrected the expert's segmentations finally, which were exploited as the ground-truth. The inter-observer variation is utilized to evaluate the relative agreement of the delineations. The inter-observer variation of HV (resp. PV) between two observers ( $o_1$  and  $o_2$ ) is  $IOV = 1/N \sum_{i=1}^N |DC_{o1,i} - DC_{o2,i}|$ , where  $N$  is number of data in all datasets, and  $DC$  is the manual segmentation performance (Dice-score). The error (i.e.,  $1 - DC$ ) of each observer

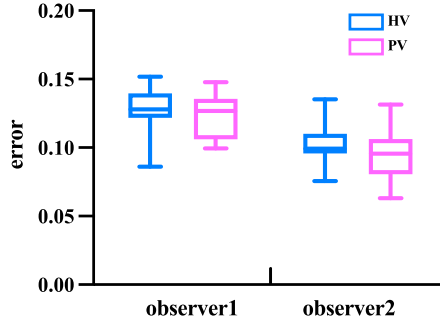


Fig. 5. Error maps of observers. The blue and the pink boxes represent the errors (i.e.,  $1 - DC$ ) of HV and PV, respectively.

is illustrated in Fig. 5, and the overall *IOV* is 3.48% by averaging the inter-observer variation of HV and PV.

2) *Evaluation Metrics*: The F1 score, precision (PRE), and sensitivity (SEN) are calculated as criteria to evaluate the intrahepatic segmentation results. F1 indicates the overall performance of the vessel segmentation, defined as:  $F1 = 2TP/(2TP + FP + FN)$ . PRE represents the method's ability to discard background voxels, computed as:  $PRE = TP/(TP + FP)$ . SEN represents the method's ability to detect vessel voxels, computed as:  $SEN = TP/(TP + FN)$ . To quantitatively measures the percentage of the correct changed and unchanged voxels, the percentage correct classification (PCC) is given by:  $PCC = (TP + PN)/(TP + FP + TN + FN)$ . FN, FP, TP, and TN represent the false negatives, false positives, true positives, and true negatives, respectively. Kappa coefficient assesses the consistency of the CD results with the reference and is defined as:  $Kappa = (po - pe)/(1 - pe)$ , where  $po$  is the observed PCC, and  $pe$  is the expected PCC [38]. Complementarily, the separation metric measures the false alarms between HV and PV segmentation result. Similar to [39], the voxel-based agreement is defined as follows:

$$agreement = \frac{|H_{ref} \cap H_{seg}| + |P_{ref} \cap P_{seg}|}{|(H_{ref} \cup P_{ref}) \cap (H_{seg} \cup P_{seg})|} \quad (24)$$

$$FNR = (P_{ref} \cap H_{seg}) / P_{ref} \quad (25)$$

$$FPR = (H_{ref} \cap P_{seg}) / H_{ref}, \quad (26)$$

where  $H_{ref}$  and  $H_{seg}$  are the sets of reference and segmentation of HV, and  $P_{ref}$  and  $P_{seg}$  are the corresponding results of PV. For segmentation and separation evaluations, the largest connected component of the PV segmentation result was applied, while the connected components included less than 200 voxels are removed for the HV segmentation result. To quantitatively analyze the performance trend and stability of the framework, the mean value and standard deviation of each metric are calculated respectively. Our experiments were carried out in python and cython on a PC with an Intel Core i5-9600K CPU, 3.7GHz, and 64GB RAM.

#### B. FGCD Study

1) *Importance of Guidance*: We examined the effectiveness of the “W/o guidance” framework by removing the JFMS steps

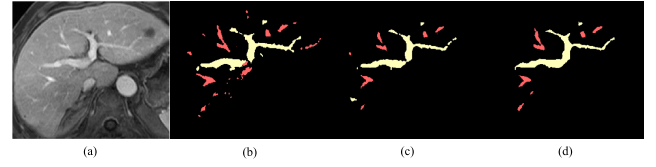


Fig. 6. Visual exemplary segmentation results of HV and PV. (a) Raw images; (b) Results of “W/o guidance” framework; (c) Results of our proposed framework; (d) ground-truth. The HV and PV are indicated in red and yellow respectively.

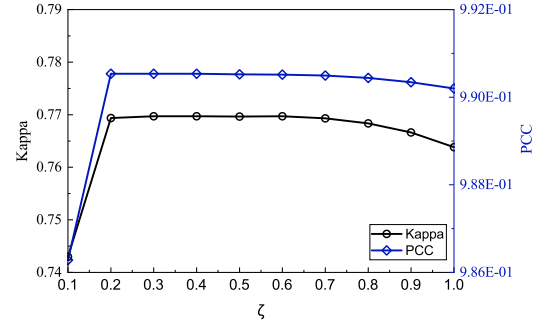


Fig. 7. Performance of framework over LHD against the parameter  $\zeta$ . The blue line (to right axis) and black line (to left axis) represents the PCC and Kappa scores, respectively.

TABLE I  
QUANTITATIVE STATISTICAL RESULTS FOR FGCD AND CDI-K. THE PERCENTAGE CORRECT CLASSIFICATION PCC AND KAPPA COEFFICIENT ARE PRESENTED AS AVERAGE  $\pm$  DEVIATION

	PCC(%)	Kappa(%)
CDI-K [16]	$67.01 \pm 34.30$	$26.09 \pm 34.00$
FGCD (ours)	$99.20 \pm 0.35$	$78.03 \pm 9.46$

of FGCD. As depicted in Table II, the PRE of HV and PV for “W/o guidance” framework is lower than that of FGCD while SEN is higher than that of our proposed framework. Remarkably, FGCD can achieve more than 14.16% increase of F1 to the HV and 15.74% increase of F1 to the PV. These observations indicate that the framework without guidance will lead to more background misjudged as vascular voxels in the final segmentation results. The HV and PV exemplary segmentation results in Fig. 6 show that without the JFMS, an effective prediction for any type of vasculature is difficult to be obtained. Instead, our framework can successfully mitigate the influence associated with the fuzzy artifacts and pseudo-vascular noise inside the liver region.

2) *The Verification of HVP map Generation Module*: The regularization parameter  $\zeta$  from 0.1 to 1 is used to quantitatively analyze the influence on the subtraction and ratio operators in FGCD. Based on HV segmentation results without post-processing, we calculate the CD metrics, i.e., Kappa and PCC scores, for all possible weight combinations at intervals of 0.1 [16], respectively. In Fig. 7, the left and right axes separately represent the Kappa and PCC index. The Kappa and PCC scores increase with the rise of  $\zeta$  at first, while if the value of  $\zeta$  becomes dramatically high, their scores will

TABLE II  
PERFORMANCE COMPARISON WITH DIFFERENT METHODS FOR HV AND PV SEGMENTATION OVER LHD.  
THE SENSITIVITY *SEN*, PRECISION *PRE*, AND *F1* SCORE ARE PRESENTED AS AVERAGE  $\pm$  DEVIATION

Method	PRE(%)		SEN(%)		F1(%)	
	HV	PV	HV	PV	HV	PV
W/o guidance	56.58 $\pm$ 21.21	55.29 $\pm$ 9.65	<b>82.95</b> $\pm$ 8.18	<b>74.55</b> $\pm$ 13.45	63.88 $\pm$ 15.95	62.73 $\pm$ 9.50
PFCM [34]	93.90 $\pm$ 12.48	<b>98.14</b> $\pm$ 2.61	35.21 $\pm$ 20.75	37.64 $\pm$ 10.43	47.50 $\pm$ 20.68	53.57 $\pm$ 11.03
VRT [35]	74.64 $\pm$ 10.94	76.98 $\pm$ 22.00	63.20 $\pm$ 12.45	54.52 $\pm$ 21.49	66.97 $\pm$ 7.93	62.49 $\pm$ 20.40
RORPO [40]	87.18 $\pm$ 7.41	71.50 $\pm$ 13.33	39.72 $\pm$ 7.07	25.45 $\pm$ 8.02	54.17 $\pm$ 7.10	36.64 $\pm$ 8.85
MTHTV [41]	<b>95.15</b> $\pm$ 10.39	97.49 $\pm$ 1.57	25.30 $\pm$ 9.61	26.73 $\pm$ 13.65	39.17 $\pm$ 13.06	40.13 $\pm$ 17.56
V-Net [42]	64.23 $\pm$ 16.21	69.26 $\pm$ 24.01	42.76 $\pm$ 23.69	53.57 $\pm$ 24.07	45.85 $\pm$ 15.43	56.42 $\pm$ 19.63
nnU-Net [43]	76.93 $\pm$ 11.73	82.67 $\pm$ 5.35	67.45 $\pm$ 10.83	62.17 $\pm$ 18.55	71.38 $\pm$ 9.47	68.91 $\pm$ 14.31
DVnet [10]	- $\pm$ -	- $\pm$ -	- $\pm$ -	- $\pm$ -	64.70 $\pm$ 5.00	60.30 $\pm$ 8.40
FGCD (ours)	88.28 $\pm$ 9.16	87.03 $\pm$ 9.43	71.10 $\pm$ 10.04	72.78 $\pm$ 11.87	78.04 $\pm$ 6.94	78.47 $\pm$ 9.34
FGCD-IDM (ours)	88.10 $\pm$ 9.06	86.92 $\pm$ 9.41	71.37 $\pm$ 10.26	72.87 $\pm$ 11.67	<b>78.13</b> $\pm$ 7.06	<b>78.51</b> $\pm$ 9.21

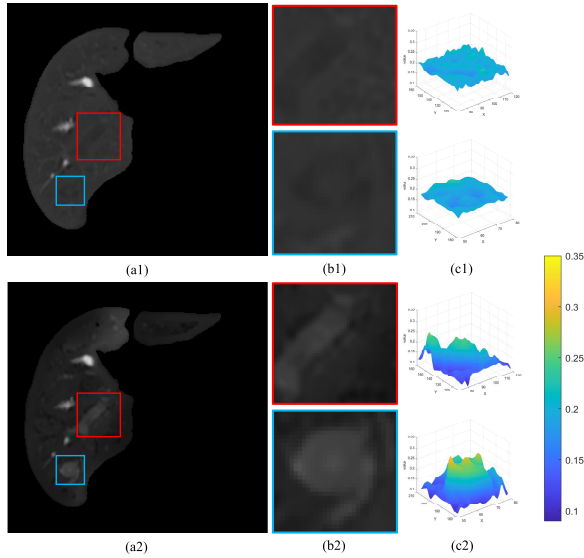


Fig. 8. The results of the HVP map generation module and the CDI module. (a1) and (a2) show the two difference maps generated by the proposed module and CDI module. The two maps are normalized to the range [0,1], (b1) and (b2) amplify the same colored boxes in (a1), (a2) to display PV (red) and tumor (blue) region. (c1) and (c2) are distribution characteristics of (b1) and (b2). The maximum and minimum values of the rightmost color bar correspond to the maximum and minimum intensity among the four patches (i.e., (b1) and (b2)), respectively.

turn low. The parameter  $\zeta$  controls the contribution of the subtraction and ratio operators. The Kappa and PCC scores are stable within a wide parameter range  $\zeta \in [0.3, 0.6]$ . Finally,  $\zeta = 0.3$  is selected as the optimal weight, under which the effect of FGCD by integrating the operators is better than that by using a unique one.

To analyze the effectiveness of FGCD, the combined difference image module with k-means clustering (CDI-K) [16] is utilized for comparison. The quantitative results for FGCD and CDI-K are summarized in Table I. The PCC score of CDI-K is lower than that of FGCD, and its Kappa score is 26.09% with 51.94% gap to FGCD, indicating that FGCD generally obtains the better detection results, and CDI finds a host of changed details unrelated to hepatic

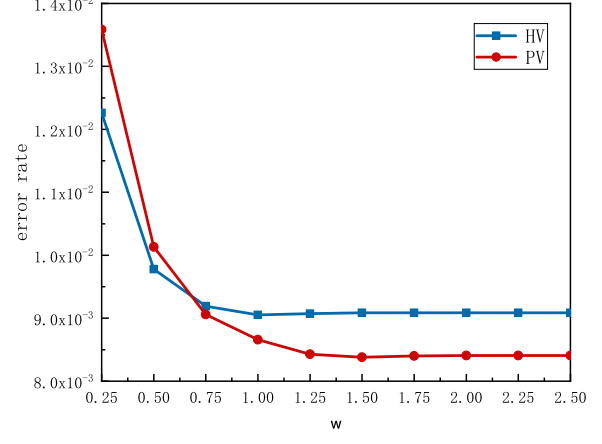


Fig. 9. Varying trend of error rate under different values of  $w$ . The blue line and the red line represent the error rate of HV and PV, respectively.

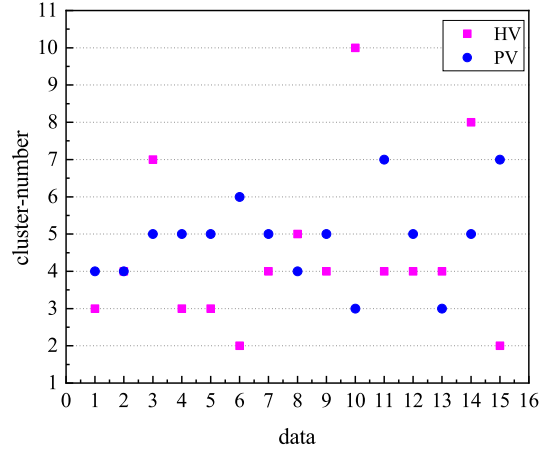


Fig. 10. The optimal cluster-number of PFCM over LHD. The blue and the pink points represent the optimal cluster-number relating to PV and HV, respectively.

venous flow between the multi-phase images. As depicted in Fig. 8, (a1) and (a2) show the two difference maps generated by the proposed module and CDI module, respectively. The results clearly demonstrate that the CDI module can

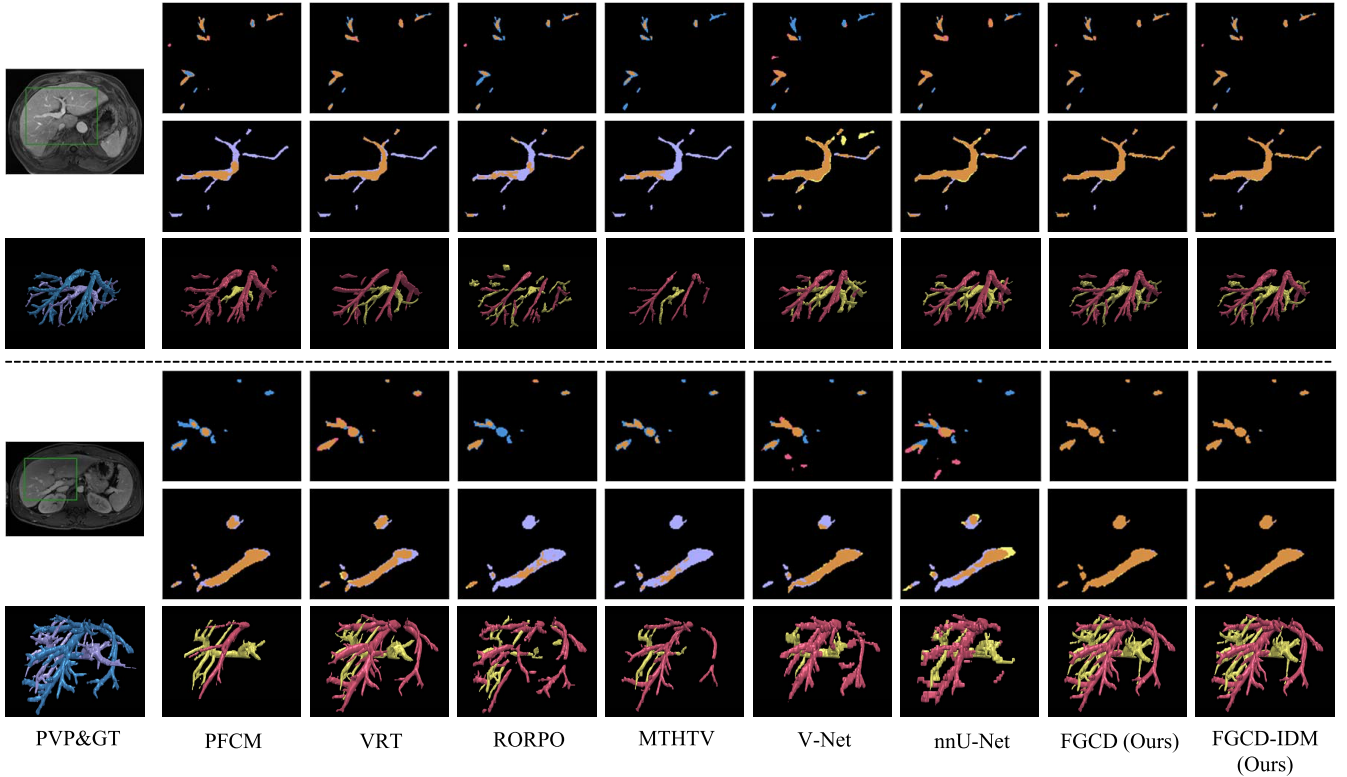


Fig. 11. Visual comparison of segmentation results of HV and PV on clinical MR images for LHD (top three rows) and TCGA (bottom three rows). From left to right are the raw PVP images and ground-truth (GT) (1st column), PFCM results (2nd column), results of vasculature-based methods (3rd-5th columns), results of deep learning-based methods (6th-7th columns), our FGCD results (8th column), and our FGCD-IDM results (last column). All 2D images are a z slice. For each slice (2nd-9th column), the HV/PV segmentation result of each method is compared with its corresponding Ground-truth, respectively. Blue - ground-truth of HV, purple - ground-truth of PV, red - HV segmentation result, yellow - PV segmentation result, orange - true positive region in the segmentation result.

obtain the changed region easily, but it is sensitive to other change information caused by the vascular flow event as well. Compared with CDI module, the difference information obtained by HVP map generation module make HV more distinguishable.

### C. Evaluation of Segmentation Performance

1) Parameter Study: Fig. 9 shows the error rate (i.e.,  $1 - PCC$ ) of HV and PV segmentation results over LHD when  $w$  varies from 0.25 to 2.5 with step 0.25. We can see from Fig. 9 that the error rate tends to be stable at  $w = 1.75$ , indicating that the increase of intensity neighborhood (i.e.  $\epsilon$ ) will not influence the segmentation performance of target vasculature in the corresponding prior space. Therefore,  $w = 1.75$  is selected as the optimal weight in our experiments for segmentation evaluation on both LHD and TCGA.

2) Evaluation of HV/PV Segmentation: Here, we compare our proposed framework with the PFCM method [34] and three vasculature-based methods, i.e., volume ratio tensor (VRT) [35], ranking the orientation responses of path operators (RORPO) [40] and vesselness of multiscale top-hat tensor (MTHTV) [41], [44] approach, for the HV and PV. The first approach is used for clustering segmentation task, while the other three methods are utilized for vascular segmentation task.

Similar to [45] and [5], the three vasculature-based methods are implemented with an optimal thresholding strategy. For a fair comparison, the boundary expansion images  $E_h$  (resp.  $E_p$ ) are used as input of methods to be compared to mitigate undesired strong contrast near liver boundary, and the same post-processing is used for these comparison methods as our method.

Besides, to evaluate the HV/PV segmentation performance of different network architectures, we compare the proposed framework with three state-of-the-art deep learning-based methods: V-Net [42], nnU-Net [43], and DVnet [10]. DVnet with focal loss is utilized as an objective benchmark of the MR-based HV/PV segmentation task, where the results originally reported by [10] are applied for comparsion. Both V-net and nnU-Net are public-accessbale architectures and developed to medical image segmentation. Based on the success of DVnet, V-net combined with focal loss to alleviate the class imbalance problem and employed additional preprocessing such as liver-specific normalization. The network is trained by exploiting the ADAM solver and random patch generation strategy with an initial learning rate of  $1.0 \times 10^{-3}$ . Due to robust applicability, nnU-Net is implemented with default settings [43]. For all supervised deep learning methods, we set the maximum training iteration to 200 epochs. In addition, similar to [46], the HV/PV segmentation results were quantified by k-fold

TABLE III

PERFORMANCE COMPARISON WITH DIFFERENT METHODS FOR HV AND PV SEGMENTATION OVER TCGA.  
THE SENSITIVITY *SEN*, PRECISION *PRE*, AND *F1* SCORE ARE PRESENTED AS AVERAGE  $\pm$  DEVIATION

Method	PRE(%)		SEN(%)		F1(%)	
	HV	PV	HV	PV	HV	PV
PFCM [34]	<b>100.</b> $\pm$ 0.00	99.56 $\pm$ 0.62	22.18 $\pm$ 1.91	45.54 $\pm$ 18.48	36.29 $\pm$ 2.55	61.35 $\pm$ 17.42
VRT [35]	78.48 $\pm$ 13.65	91.28 $\pm$ 6.19	7.13 $\pm$ 1.37	62.26 $\pm$ 1.23	74.38 $\pm$ 5.47	73.96 $\pm$ 1.16
RORPO [40]	87.42 $\pm$ 13.39	85.57 $\pm$ 2.08	37.78 $\pm$ 2.38	18.56 $\pm$ 3.23	52.50 $\pm$ 0.15	30.46 $\pm$ 4.49
MTHTV [41]	99.90 $\pm$ 0.02	<b>99.94</b> $\pm$ 0.03	35.01 $\pm$ 0.50	15.12 $\pm$ 1.35	51.85 $\pm$ 0.54	26.26 $\pm$ 2.03
V-Net [42]	63.74 $\pm$ 18.11	53.40 $\pm$ 28.85	40.02 $\pm$ 17.34	50.00 $\pm$ 22.28	44.42 $\pm$ 11.91	46.37 $\pm$ 16.70
nnU-Net [43]	62.58 $\pm$ 2.95	82.21 $\pm$ 4.65	66.22 $\pm$ 16.59	47.33 $\pm$ 7.98	63.16 $\pm$ 7.21	59.70 $\pm$ 6.34
DVnet [10]	- $\pm$ -	- $\pm$ -	- $\pm$ -	- $\pm$ -	64.70 $\pm$ 5.00	60.30 $\pm$ 8.40
FGCD (ours)	89.82 $\pm$ 11.44	85.15 $\pm$ 15.61	90.60 $\pm$ 3.65	93.02 $\pm$ 0.26	89.89 $\pm$ 3.97	88.55 $\pm$ 8.66
FGCD-IDM (ours)	89.83 $\pm$ 11.41	85.17 $\pm$ 15.60	<b>90.81</b> $\pm$ 3.94	<b>93.18</b> $\pm$ 0.30	<b>89.99</b> $\pm$ 3.83	<b>88.63</b> $\pm$ 8.68

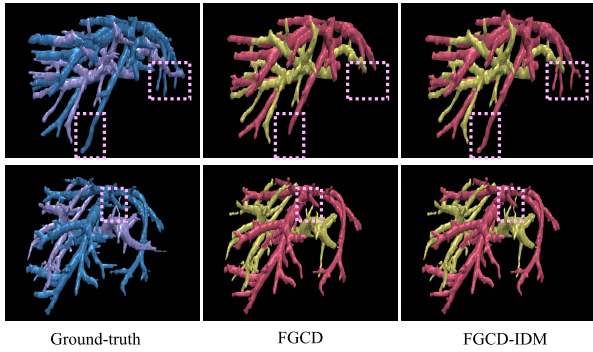


Fig. 12. The 3D HV and PV visualization for FGCD and FGCD-IDM. Blue - ground-truth of HV, purple - ground-truth of PV, red - HV segmentation result, yellow - PV segmentation result. The pink dotted box indicates the refinement regions.

( $k = 5$ ) cross-validation. Training and testing PVP datasets are divided randomly from the LHD and applied to the  $k$ -fold cross-validation. Based on the  $k$  trained models, each PVP data of TCGA is tested to obtain average evaluation metrics. Similarly, to be equitable, the same post-processing as our method is used for these comparison methods. At last, to show the effectiveness of IDM in our framework, the discussion about FGCD and FGCD-IDM are provided.

Table II reports the HV and PV segmentation results on clinical MR images of LHD. As can be seen, a performance gap remains between PFCM utilizing the average optimal cluster-number and our proposed FGCD with 30.54% F1 gap for the HV and 24.90% F1 gap for the PV. The cluster-number uncertainty of PFCM is a major factor that induces its unreliable segmentation problem. This is because the cluster-number selection is hard to be reasonably explained by PFCM for real-patient dataset. As shown in Fig. 10, the optimal cluster-number points of PFCM for all patient data present an obvious fluctuating range. However, FGCD specifies the fixed cluster-number relating to HV and PV while maintaining effective performance. It divides all voxels into target vascular (resp. changed) cluster and background (resp. non-changed) cluster. The VRT method has better segmentation performance than other vasculature-based (such

as RORPO and MTHTV) methods, which can capture vascular feature and detect a vast majority of target vasculature. However, the major problem of VRT is distinguishing vascular fuzzy boundaries from confounding tissue, as depicted in Fig. 11 (top three rows). Notably, FGCD outperformed the three supervised methods (i.e., V-Net, nnU-Net, and DVnet) for HV/PV segmentation without relying on the ground truth of HV/PV. This is primarily owing to: 1) FGCD discriminates and captures the global information related to vascular flow by designing the HVP map generation and shared clustering module, which can yield more continuous and integral HV/PV segmentation results. 2) The interpretability of single-phase data with complex topologies is challenging for these supervised methods. 3) Small training datasets, especially those acquired on multi-scanners, may hamper the performance of CNN networks.

Correspondingly, Table III presents the HV and PV segmentation results over TCGA. Similar to Table II, FGCD and FGCD-IDM significantly outperform all the compared methods on HV/PV segmentation performance. To be more comprehensive, the bottom three rows of Fig. 11 visualizes the details of HV and PV segmentation results on clinical MR images of TCGA.

Furthermore, compared with FGCD, FGCD-IDM over both LHD and TCGA obtain better F1 scores on HV and PV, respectively. The increase in segmentation performance demonstrates that the IDM can reduce false alarms after the shared clustering. We further qualitatively compare the effect of IDM and show the 3D HV/PV segmentation results of two samples in Fig. 12, where pink dotted boxes of the top row and the bottom row indicate the HV (red) and PV (yellow) refinement region, respectively.

3) *Evaluation of Intrahepatic Vascular Segmentation:* To analyze the performance of intrahepatic vascular segmentation over LHD and TCGA, we first combine the HV and PV segmentation results of FGCD and those of FGCD-IDM, respectively. Then, the two combined results are compared with the segmentation results of the three vasculature-based (e.g., VRT, RORPO, and MTHTV) methods from a single-phase image, i.e. the PVP image. For a fair comparison, the boundary expansion image  $E_b$  is applied to the methods to be compared.

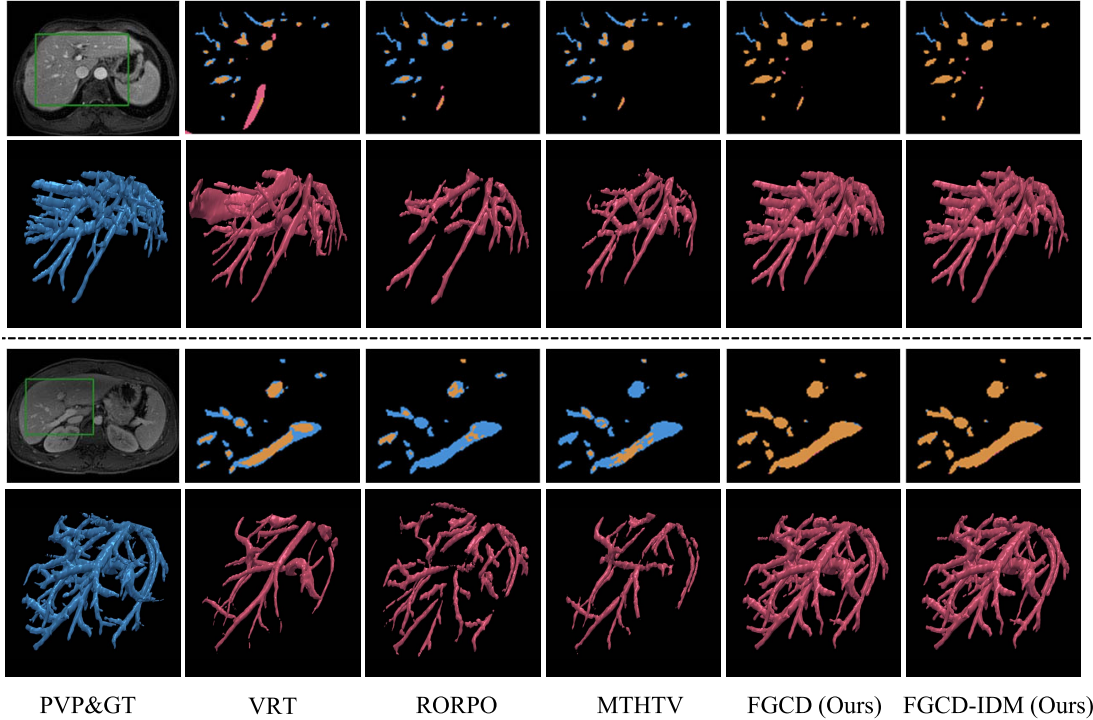


Fig. 13. Visual comparison of the intrahepatic vascular segmentation results over LHD (top two rows) and TCGA (bottom two rows). From left to right are the raw PVP images and ground-truth (GT) (1st column), the results of vasculature-based methods (2nd-4th column), our FGCD results (5th column), our FGCD-IDM results (last column). All 2D images are a z slice. For each slice (2nd-6th column), the HV/PV segmentation result of each method is compared with its corresponding ground-truth, respectively. Blue - ground-truth, red - segmentation result in the segmentation result.

Tables IV and V present the segmentation results of intrahepatic vasculature on the clinical MR images of LHD and TCGA, respectively. In comparison with the FGCD, the F1 scores of FGCD-IDM increase to 79.12% over LHD and 91.26% over TCGA, demonstrating that IDM can remove non-vascular noise besides false alarms between HV and PV. Table IV shows that the PRE, SEN, and F1 obtained by FGCD-IDM were 87.94%, 72.36%, and 79.12%, respectively. In comparison with VRT, RORPO and MTHTV methods, the proposed method demonstrates the highest score for F1 evaluation metrics, indicating that the proposed method can adequately segment intrahepatic vasculature on the MR images. Simultaneously, making full use of multi-phase information is conducive to intrahepatic vascular segmentation. Consistent with the aforementioned analysis over LHD, we observe that the segmentation performance of intrahepatic vasculature of both FGCD and FGCD-IDM outperform other comparison approaches by a large margin over the TCGA, as can be seen in Table V. Fig. 13 shows the intrahepatic vascular segmentation results over the TCGA and LHD. In Fig. 13, the images clearly show that more accurate vascular voxels in the proposed segmentation result are obtained than those in other comparison methods, which validates the proposed method is more effective to segment vasculature.

#### D. Evaluation of Separation Performance

The separation strategy had been undertaken in [39] [47], where an objective scheme of this classified assessment

TABLE IV  
PERFORMANCE COMPARISON WITH DIFFERENT METHODS FOR INTRAHEPATIC VASCULAR SEGMENTATION OVER LHD. THE SENSITIVITY *SEN*, PRECISION *PRE*, AND *F1* SCORE ARE PRESENTED AS AVERAGE  $\pm$  DEVIATION

Method	<i>PRE</i> (%)	<i>SEN</i> (%)	<i>F1</i> (%)
VRT [35]	$70.51 \pm 16.33$	$35.44 \pm 10.66$	$45.67 \pm 9.53$
RORPO [40]	$85.91 \pm 6.92$	$25.17 \pm 4.25$	$38.66 \pm 4.77$
MTHTV [41]	<b><math>92.88 \pm 5.60</math></b>	$20.18 \pm 8.67$	$32.25 \pm 12.20$
FGCD (ours)	$88.01 \pm 6.90$	$72.16 \pm 7.58$	$79.03 \pm 5.94$
FGCD-IDM (ours)	$87.94 \pm 6.83$	<b><math>72.36 \pm 7.73</math></b>	<b><math>79.12 \pm 6.02</math></b>

considered the voxels both in arteries and veins of the brain only. Therefore, inspired by [39] [47], the FNR, FPR, and agreement were used to provide the quantitative evaluation of HV and PV from all datasets (LHD and TCGA) to avoid the over-segmentation impact between HV and PV. The quantitative performance of our framework is presented in Table VI. To be more comprehensive, the visual 2D and 3D results are shown in Figs. 11 and 12. Our framework can automatically separate HV and PV, which is not limited by the irregular tubular shape and unconventional bifurcation structure.

#### E. Robustness Discussion

To verify the robustness of the 3D HV and PV segmentation framework, more discussion is presented on the segmentation of the clinical MR data including the significant artifacts, deformations, displacements, and low resolution, etc. As shown in Fig. 14, compared the LAP image with

TABLE V

PERFORMANCE COMPARISON WITH DIFFERENT METHODS FOR INTRAHEPATIC VASCULAR SEGMENTATION OVER TCGA. THE SENSITIVITY *SEN*, PRECISION *PRE*, AND *F1* SCORE ARE PRESENTED AS AVERAGE  $\pm$  DEVIATION

Method	<i>PRE</i> (%)	<i>SEN</i> (%)	<i>F1</i> (%)
VRT [35]	87.74 $\pm$ 5.88	44.68 $\pm$ 19.59	57.51 $\pm$ 16.04
RORPO [40]	86.57 $\pm$ 11.23	20.97 $\pm$ 5.70	33.34 $\pm$ 6.51
MTHTV [41]	<b>94.67</b> $\pm$ 1.34	28.18 $\pm$ 13.04	42.66 $\pm$ 15.72
FGCD (ours)	90.91 $\pm$ 8.90	91.78 $\pm$ 2.42	91.17 $\pm$ 3.30
FGCD-IDM (ours)	90.92 $\pm$ 8.89	<b>91.95</b> $\pm$ 2.56	<b>91.26</b> $\pm$ 3.23

TABLE VI

QUANTITATIVE EVALUATION OF SEPARATION FOR HV AND PV

	FNR(%)	FPR(%)	Agreement(%)
Average	2.23	0.32	99.18
Std	5.75	0.54	2.62

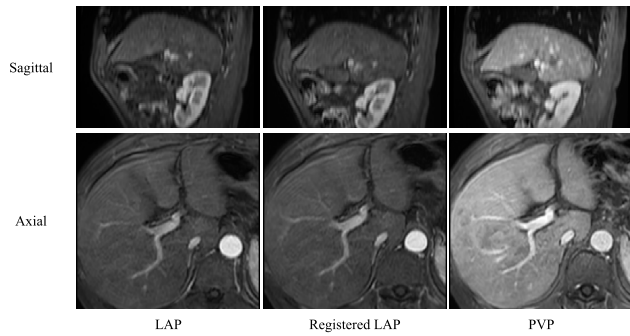


Fig. 14. One clinical MR data of LHD with significant artifacts, deformations, displacements, and low resolution, etc.

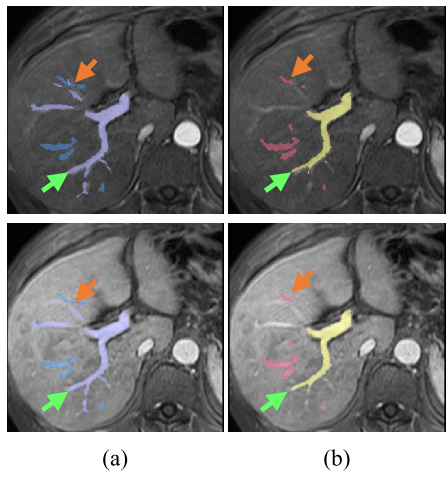


Fig. 15. The registered LAP (top row) and PVP (bottom row) with labeled vessels. Blue - ground-truth of HV from PVP, purple - ground-truth of PV from PVP, red - HV segmentation result, yellow - PV segmentation result. The orange and green arrows point to HV and PV branches, respectively.

the PVP image, the displacement, and artifacts of the liver tissue occur on the Sagittal and Axial image, respectively, and the deformation of the intrahepatic tissue is reflected on both images. Although the registration is utilized in

the preprocessing step, artifacts remain on the registered LAP image, and the appearance (i.e., structural and textural information) of the co-registered LAP and PVP is not exactly consistent. However, in Fig. 15, the main branches of HV and PV can be segmented from the complex background, especially the HV branch suffering from the artifacts (e.g. orange arrows on Fig. 15). The main reason for missing PV branches is the loss of vascular flow information in the adjacent slices after registration. Specifically, the slice thickness in the z-axis of our dataset is considerable, resulting in the lower resolution of the Sagittal image than that of the Axial image (e.g. Fig. 14). For fuzzy and thin vascular branches, their spatial information related to vascular flow is unable to ensure integrity after rough registration. Similar to most CD methods [48], image registration is another meaningful research subject. Consequently, with the fixed-parameter settings, the general non-rigid registration method was conducted as a preprocessing step. It is worth noting that our framework can capture the real structure of target vasculature without relying on strict co-registration images (e.g. green arrows on Fig. 15).

## V. CONCLUSION

In this paper, we proposed a novel vascular segmentation framework, named FGCD-IDM. Our FGCD-IDM is able to extract 3D HV and PV in unison, by modelling both the change and appearance caused by the vascular flow event between MR images of different phases. The experimental results over TCGA and LHD have demonstrated that the proposed framework can effectively segment HV, PV, and intrahepatic vasculature. Our results confirm its potential as a new segmentation strategy to analyze intrahepatic vasculature from clinical MR images. Moreover, our work makes a step towards the extended application of biomedical change detection, namely, building bridges between the change problem and the venous flow event.

Although this paper underlines the potential for our proposed FGCD-IDM to segment HV and PV, there remain several improvement aspects. Lesions regions with tube-like features can make our framework over-segment these regions. This limitation could be addressed by introducing assistant information, for instance, the feature constraints from multi-phase fusion. In addition, we will exploit other phases to address artery segmentation, therefore further improving the performance of the proposed method. In the future, we will design a novel segmentation framework for extending the applications of biomedical change detection on other phases of MR images or other modality images involving multiple phases.

## COMPLIANCE WITH ETHICAL STANDARDS

Approval was granted by the Ethics Committee of Chinese PLA General Hospital (Date November, 2020/No. 2020-464-01).

## REFERENCES

- [1] S. Young, A. Taylor, and T. Sanghi, "Post locoregional therapy treatment imaging in hepatocellular carcinoma patients: A literature-based review," *J. Clin. Transl. Hepatol.*, vol. 6, no. 2, pp. 189–197, 2018.

- [2] C. Couinaud and L. Foie, *Études Anatomiques et Chirurgicales*. Paris, France: Mason, 1957, pp. 400–409.
- [3] J.-P. Dou *et al.*, “Outcomes of microwave ablation for hepatocellular carcinoma adjacent to large vessels: A propensity score analysis,” *Oncotarget*, vol. 8, no. 17, pp. 28758–28768, Apr. 2017.
- [4] E. Goceri, “Automatic labeling of portal and hepatic veins from MR images prior to liver transplantation,” *Int. J. Comput. Assist. Radiol. Surg.*, vol. 11, no. 12, pp. 2153–2161, Dec. 2016.
- [5] M.-A. Lebre *et al.*, “Automatic segmentation methods for liver and hepatic vessels from CT and MRI volumes, applied to the Couinaud scheme,” *Comput. Biol. Med.*, vol. 110, pp. 42–51, Jul. 2019.
- [6] X. Kang, Q. Zhao, K. Sharma, R. Shekhar, B. J. Wood, and M. G. Linguraru, “Automatic labeling of liver veins in CT by probabilistic backward tracing,” in *Proc. IEEE 11th Int. Symp. Biomed. Imag. (ISBI)*, Apr. 2014, pp. 1115–1118.
- [7] Y.-Z. Zeng, Y. Q. Zhao, and P. Tang, “Liver vessel segmentation and identification based on oriented flux symmetry and graph cuts,” *Comput. Methods Programs Biomed.*, vol. 150, pp. 31–39, Oct. 2017.
- [8] Z. Yan, F. Chen, and D. Kong, “Liver venous tree separation via twin-line RANSAC and Murray’s law,” *IEEE Trans. Med. Imag.*, vol. 36, no. 9, pp. 1887–1900, Sep. 2017.
- [9] W. Yu, B. Fang, Y. Liu, M. Gao, S. Zheng, and Y. Wang, “Liver vessels segmentation based on 3D residual U-Net,” in *Proc. IEEE Int. Conf. Image Process. (ICIP)*, Sep. 2019, pp. 250–254.
- [10] O. V. Ivashchenko, Z. Zhai, B. C. Stoel, and T. J. Ruers, “Optimization of hepatic vasculature segmentation from contrast-enhanced MRI, exploring two 3D Unet modifications and various loss functions,” in *Medical Imaging: Image-Guided Procedures, Robotic Interventions, and Modeling*, vol. 11598. Bellingham, WA, USA: SPIE, 2021, Art. no. 115980J.
- [11] D. Keshwani, Y. Kitamura, S. Ihara, S. Iizuka, and E. Simo-Serra, “TopNet: Topology preserving metric learning for vessel tree reconstruction and labelling,” in *Proc. Int. Conf. Med. Image Comput. Comput.-Assist. Intervent.* Cham, Switzerland: Springer, 2020, pp. 14–23.
- [12] T. Alhonnoro *et al.*, “Vessel segmentation for ablation treatment planning and simulation,” in *Proc. Int. Conf. Med. Image Comput. Comput.-Assist. Intervent.* Berlin, Germany: Springer, 2010, pp. 45–52.
- [13] O. V. Ivashchenko *et al.*, “A workflow for automated segmentation of the liver surface, hepatic vasculature and biliary tree anatomy from multiphase MR images,” *Magn. Reson. Imag.*, vol. 68, pp. 53–65, May 2020.
- [14] X. Bai, Y. Zhang, H. Liu, and Z. Chen, “Similarity measure-based probabilistic FCM with label information for brain MRI segmentation,” *IEEE Trans. Cybern.*, vol. 49, no. 7, pp. 2618–2630, Jul. 2019.
- [15] R. J. Radke, S. Andra, O. Al-Kofahi, and B. Roysam, “Image change detection algorithms: A systematic survey,” *IEEE Trans. Image Process.*, vol. 14, no. 3, pp. 294–307, Mar. 2005.
- [16] Y. Zheng, X. Zhang, B. Hou, and G. Liu, “Using combined difference image and k-means clustering for SAR image change detection,” *IEEE Geosci. Remote Sens. Lett.*, vol. 11, no. 3, pp. 691–695, Mar. 2014.
- [17] P. Shao, W. Shi, P. He, M. Hao, and X. Zhang, “Novel approach to unsupervised change detection based on a robust semi-supervised FCM clustering algorithm,” *Remote Sens.*, vol. 8, no. 3, p. 264, 2016.
- [18] Y. Zheng, L. Jiao, H. Liu, X. Zhang, B. Hou, and S. Wang, “Unsupervised saliency-guided SAR image change detection,” *Pattern Recognit.*, vol. 61, pp. 309–326, Jan. 2017.
- [19] Z. Liu, G. Li, G. Mercier, Y. He, and Q. Pan, “Change detection in heterogenous remote sensing images via homogeneous pixel transformation,” *IEEE Trans. Image Process.*, vol. 27, no. 4, pp. 1822–1834, Apr. 2018.
- [20] L. Liu, Z. Jia, J. Yang, and N. K. Kasabov, “SAR image change detection based on mathematical morphology and the K-means clustering algorithm,” *IEEE Access*, vol. 7, pp. 43970–43978, 2019.
- [21] Ž. Lesjak, F. Pernuš, B. Likar, and Ž. Špiclin, “Validation of white-matter lesion change detection methods on a novel publicly available MRI image database,” *Neuroinformatics*, vol. 14, no. 4, pp. 403–420, Oct. 2016.
- [22] E. Dufresne, D. Fortun, B. Kumar, S. Kremer, and V. Noblet, “Joint registration and change detection in longitudinal brain MRI,” in *Proc. IEEE 17th Int. Symp. Biomed. Imag. (ISBI)*, Apr. 2020, pp. 104–108.
- [23] E. Goceri, Z. K. Shah, and M. N. Gurcan, “Vessel segmentation from abdominal magnetic resonance images: Adaptive and reconstructive approach,” *Int. J. Numer. Methods Biomed. Eng.*, vol. 33, no. 4, p. e2811, Apr. 2017.
- [24] A. Virzi *et al.*, “Segmentation of pelvic vessels in pediatric MRI using a patch-based deep learning approach,” in *Data Driven Treatment Response Assessment and Preterm, Perinatal, and Paediatric Image Analysis*. Cham, Switzerland: Springer, 2018, pp. 97–106.
- [25] G. Tetteh *et al.*, “DeepVesselNet: Vessel segmentation, centerline prediction, and bifurcation detection in 3-D angiographic volumes,” 2018, *arXiv:1803.09340*.
- [26] F. Zhao *et al.*, “Semi-supervised cerebrovascular segmentation by hierarchical convolutional neural network,” *IEEE Access*, vol. 6, pp. 67841–67852, 2018.
- [27] S. Zhou *et al.*, “Statistical intensity-and shape-modeling to automate cerebrovascular segmentation from TOF-MRA data,” in *Proc. Int. Conf. Med. Image Comput. Comput.-Assist. Intervent.* Cham, Switzerland: Springer, 2019, pp. 164–172.
- [28] S. Zhou *et al.*, “Segmentation of brain magnetic resonance angiography images based on MAP-MRF with multi-pattern neighborhood system and approximation of regularization coefficient,” *Med. Image Anal.*, vol. 17, no. 8, pp. 1220–1235, Dec. 2013.
- [29] N. J. Tustison *et al.*, “N4ITK: Improved N3 bias correction,” *IEEE Trans. Med. Imag.*, vol. 29, no. 6, pp. 1310–1320, Jun. 2010.
- [30] K. Marstal, F. Berendsen, M. Staring, and S. Klein, “SimpleElastix: A user-friendly, multi-lingual library for medical image registration,” in *Proc. IEEE Conf. Comput. Vis. Pattern Recognit. Workshops (CVPRW)*, Jun. 2016, pp. 134–142.
- [31] H. Donato, M. França, I. Candelária, and F. Caseiro-Alves, “Liver MRI: From basic protocol to advanced techniques,” *Eur. J. Radiol.*, vol. 93, pp. 30–39, Aug. 2017.
- [32] X. Shen, C. Zhou, L. Xu, and J. Jia, “Mutual-structure for joint filtering,” *Int. J. Comput. Vis.*, vol. 125, nos. 1–3, pp. 19–33, Dec. 2017.
- [33] R. Krishnapuram and J. M. Keller, “A possibilistic approach to clustering,” *IEEE Trans. Fuzzy Syst.*, vol. 1, no. 2, pp. 98–110, May 1993.
- [34] N. R. Pal, K. Pal, J. M. Keller, and J. C. Bezdek, “A possibilistic fuzzy C-means clustering algorithm,” *IEEE Trans. Fuzzy Syst.*, vol. 13, no. 4, pp. 517–530, Aug. 2005.
- [35] T. Jerman, F. Pernuš, B. Likar, and Ž. Špiclin, “Enhancement of vascular structures in 3D and 2D angiographic images,” *IEEE Trans. Med. Imag.*, vol. 35, no. 9, pp. 2107–2118, Sep. 2016.
- [36] B. S. Y. Lam, Y. Gao, and A. W.-C. Liew, “General retinal vessel segmentation using regularization-based multiconcavity modeling,” *IEEE Trans. Med. Imag.*, vol. 29, no. 7, pp. 1369–1381, Jul. 2010.
- [37] X. Bai, Y. Zhang, H. Liu, and Y. Wang, “Intuitionistic center-free FCM clustering for MR brain image segmentation,” *IEEE J. Biomed. Health Informat.*, vol. 23, no. 5, pp. 2039–2051, Sep. 2019.
- [38] R. Touati, M. Mignotte, and M. Dahmane, “Multimodal change detection in remote sensing images using an unsupervised pixel pairwise-based Markov random field model,” *IEEE Trans. Image Process.*, vol. 29, pp. 757–767, 2020.
- [39] C. Payer *et al.*, “Automated integer programming based separation of arteries and veins from thoracic CT images,” *Med. Image Anal.*, vol. 34, pp. 109–122, Dec. 2016.
- [40] O. Merveille, H. Talbot, L. Najman, and N. Passat, “Curvilinear structure analysis by ranking the orientation responses of path operators,” *IEEE Trans. Pattern Anal. Mach. Intell.*, vol. 40, no. 2, pp. 304–317, Feb. 2018.
- [41] C. Sazak, C. Nelson, and B. Obara, “The multiscale bowler-hat transform for blood vessel enhancement in retinal images,” *Pattern Recognit.*, vol. 88, pp. 739–750, Apr. 2019.
- [42] F. Milletari, N. Navab, and S.-A. Ahmadi, “V-Net: Fully convolutional neural networks for volumetric medical image segmentation,” in *Proc. 4th Int. Conf. 3D Vis. (3DV)*, Oct. 2016, pp. 565–571.
- [43] F. Isensee, P. F. Jaeger, S. A. A. Kohl, J. Petersen, and K. H. Maier-Hein, “nnU-Net: A self-configuring method for deep learning-based biomedical image segmentation,” *Nature Methods*, vol. 18, no. 2, pp. 203–211, Dec. 2020.
- [44] S. S. Alharbi, C. Sazak, C. J. Nelson, and B. Obara, “Curvilinear structure enhancement by multiscale top-hat tensor in 2D/3D images,” in *Proc. IEEE Int. Conf. Bioinf. Biomed. (BIBM)*, Dec. 2018, pp. 814–822.
- [45] J. Zhang, Y. Gao, S. H. Park, X. Zong, W. Lin, and D. Shen, “Structured learning for 3-D perivascular space segmentation using vascular features,” *IEEE Trans. Biomed. Eng.*, vol. 64, no. 12, pp. 2803–2812, Dec. 2017.
- [46] F. Guo *et al.*, “Improving cardiac MRI convolutional neural network segmentation on small training datasets and dataset shift: A continuous kernel cut approach,” *Med. Image Anal.*, vol. 61, Apr. 2020, Art. no. 101636.

- [47] N. Li, S. Zhou, Z. Wu, B. Zhang, and G. Zhao, "Statistical modeling and knowledge-based segmentation of cerebral artery based on TOF-MRA and MR-T1," *Comput. Methods Programs Biomed.*, vol. 186, Apr. 2020, Art. no. 105110.
- [48] F. Liu, X. Tang, X. Zhang, L. Jiao, and J. Liu, "Large-scope PolSAR image change detection based on looking-around-and-into mode," *IEEE Trans. Geosci. Remote Sens.*, vol. 59, no. 1, pp. 363–378, Jan. 2021.



**Qing Guo** received the M.S. degree in mechanical engineering from the Beijing University of Posts and Telecommunications, China, in 2018. She is currently pursuing the Ph.D. degree with the School of Computer, Beijing Institute of Technology. Her research interests include medical image analysis, machine learning, and computer vision.



**Danni Ai** received the Ph.D. degree from Ritsumeikan University, Japan, in 2011. She is currently an Associate Professor with the School of Optics and Photonics, Beijing Institute of Technology. Her research interests include medical image analysis, surgical navigation, virtual reality, and augmented reality.



**Yuanjin Gao** received the Ph.D. degree in imaging and nuclear medicine from the Graduate School of PLA General Hospital in 2021. He is currently a Physician of the Ultrasound Department, Beijing Children's Hospital, Capital Medical University. He focuses his research interests on medical image analysis, surgical navigation, medical image processing.



**Hong Song** received the Ph.D. degree in computer science from the Beijing Institute of Technology, China, in 2004. She is currently a Professor with the School of Computer Science and Technology, Beijing Institute of Technology. Her research interests focus on medical image processing, augmented reality, and computer vision.



**Xiaoling Yu** received the Ph.D. degree in imaging and nuclear medicine from the Postgraduate Medical School of PLA, China, in 2004. She is currently a Chief Physician with the Interventional Ultrasound Department, PLA General Hospital. Her research interests include interventional ultrasound in treatment and diagnosis and molecular imaging.



**Jingfan Fan** received the Ph.D. degree in optical engineering from the Beijing Institute of Technology in 2016. He worked as a Postdoctoral Researcher with the University of North Carolina at Chapel Hill, from 2017 to 2019. He is currently an Associate Professor with the School of Optics and Photonics, Beijing Institute of Technology. He focuses his research interests on medical image processing, computer vision, and augmented reality.



**Jian Yang** received the Ph.D. degree in optical engineering from the Beijing Institute of Technology, Beijing, China, in 2007. He is currently a Professor with the School of Optics and Photonics, Beijing Institute of Technology. His research interests focus on medical image processing, augmented reality, and computer vision.